Organophosphorus Binding Thermodynamics in Metal–Organic Frameworks: Interplay Between Oxidation State, Lewis Acidity, and Node Structure

Kira M. Fahy,[1] Bang Hou,[1] Palak Garg,[1] Seryeong Lee,[1] Courtney S. Smoljan,[2] Mohammad K. Shehab,[1] Kent O. Kirlikovali,[1] Omar K. Farha[1]*

[1] Department of Chemistry and International Institute for Nanotechnology (IIN), Northwestern University, Evanston, Illinois 60208, USA

[2] Department of Chemical and Biochemical Engineering, Northwestern University, 2145 Sheridan Road, Evanston, Illinois 60208, USA

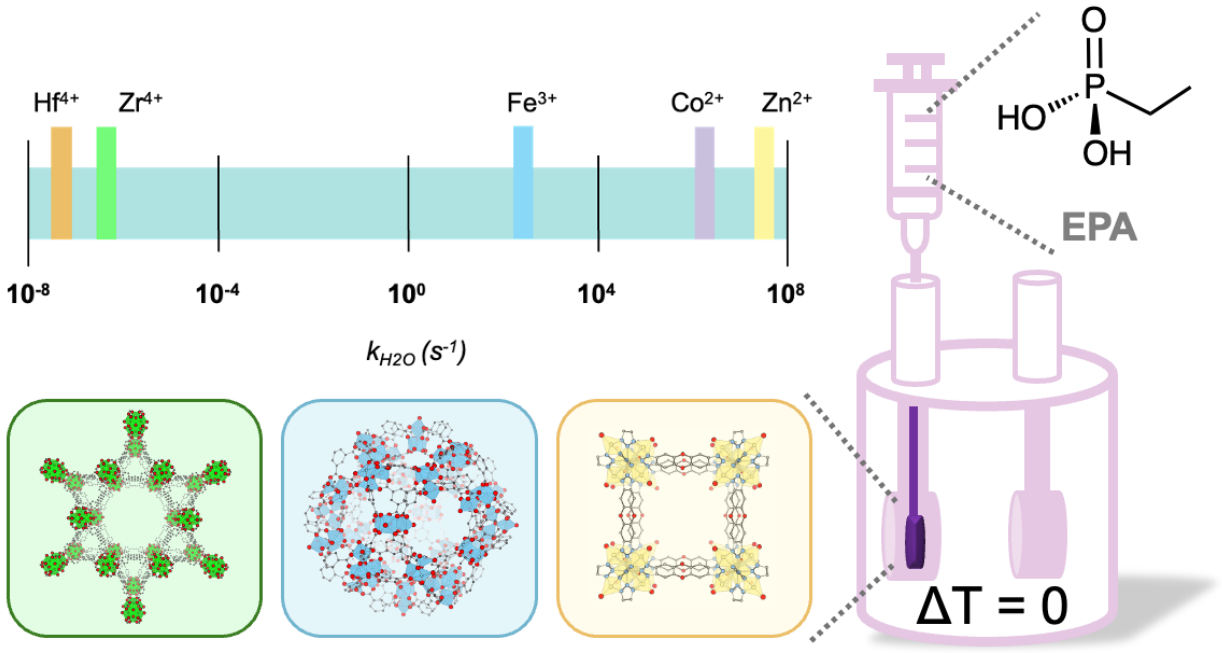

ABSTRACT:

Organophosphorus compounds, including nerve agents and pesticides, represent a class of toxic chemicals causing harm to troops, civilians, and the environment. Metal–organic frameworks (MOFs) have emerged as a class of highly porous, crystalline, tunable materials adept at both capturing and catalytically neutralizing these harmful toxins. In particular, MOFs whose nodes display strong Lewis acidic character are able to hydrolyze such chemicals nearly instantaneously. However, without the help of a basic buffer to regenerate the active site, the benign organophosphorus product strongly binds to the node and prevents catalyst turnover. Here, we investigate a series of MOFs whose nodes contain metals of varying Lewis acidities and employ isothermal titration calorimetry (ITC) to directly measure the heat from the binding of an organophosphorus probe molecule, allowing the construction of a full thermodynamic binding profile (ΔH, ΔS, ΔG, K_a). We couple this with potentiometric titrations and solid state ^{31}P magic angle spinning (MAS) NMR to gain a clearer picture of how node identity, structure, and Lewis acidity interplay to impact binding strength and favorability.

INTRODUCTION:

Metal–organic frameworks (MOFs) are a class of highly porous, crystalline materials formed by the self-assembly of multitopic organic linkers with inorganic metal ions or clusters.[1] Their modular structures enable precise control over their physical and chemical properties, such as topology,[2,3] pore size,[4–6] pore environment,[7–9] and surface features.[10] Thus, they can be tailored for specific applications and, indeed, have been adopted for applications ranging from hydrogen storage[11,12] and carbon capture[13–15] to drug delivery[16–18] and sensing.[19–21] Among these applications, catalysis has emerged as an exciting avenue, with MOFs demonstrating remarkable

activity in various chemical transformations, including oxidation, hydrogenation, and hydrolysis.[22–25]

One area of interest over the last several decades is the use of MOF catalysts for the hydrolysis of chemical warfare agents (CWAs), particularly organophosphorus nerve agents.[25–27] These are highly toxic chemicals that, while banned for use internationally, still pose significant threats to both civilian and military populations through unsanctioned use and stockpiling.[28–31] Typical materials for the capture and/or neutralization of these chemicals include amorphous metal oxides and weakly adsorbing activated carbon.[32,33] MOFs offer advantages over these materials in their inherent ability to both capture and detoxify CWAs on contact. Furthermore, the processability of MOFs allows them to be incorporated into support materials, further facilitating their real-word implementation. Several MOFs have been investigated for their hydrolysis activity, most notably Zr-based MOFs such as NU-1000, NU-901, and MOF-808.[25,26,34] The highly Lewis acidic metal-oxo node effectively draws electron density from the molecule. This weakens the potent P-F bond, which cleaves to give the benign organophosphate product and HF. While the Zr node exhibits high Lewis acidity, its propensity to strongly bind the phosphate product limits catalyst turnover.[35] The Lewis acidity plays a role in this rate-limiting step as well as the Zr ion's water exchange rate (k_{H2O}), which is often conversely related to a metal ion's acidic properties. This phenomenon describes how readily one water molecule can replace an aqua ligand within a metal-aqua complex and depends on the properties of ion such as charge density, ionic radius, and ligand field effects.[36,37] Thus, a careful balance must be struck between Lewis acidity and water exchange rate to ensure optimal catalytic performance.

Understanding the binding interactions at a molecular level, including the impact of Lewis acidity and water exchange rate, is crucial for designing next-generation MOFs with improved

catalytic performance. Isothermal titration calorimetry (ITC) is a powerful tool for quantifying these interactions and providing direct measurements for binding affinity and thermodynamic parameters. ITC is most commonly used in biology fields to study protein/ligand interactions or other homogeneous systems; however, recently it has been adopted to the heterogeneous community with early success in measuring MOF/protein binding,[38,39] catalyst/substrate interaction,[40] and composite material formation.[41] In a typical set-up, the analyte is loaded into a syringe connected to a highly temperature-sensitive cell containing the material of interest. Adjacent to this is the reference cell, an identical chamber filled with water or buffer. The analyte is titrated in small volumes into the cell containing the material of interest, leading to a binding interaction that either releases or absorbs heat based on the mechanism. A minuscule temperature change occurs, and the reference cell adjusts its temperature to match that of the sample cell. Recorded by the instrument is the power needed by the ITC to adjust the temperature of the reference cell. As the system saturates, these peaks plateau. They can then be integrated and plotted against the mole ratio, resulting in a sigmoidal binding curve from which the binding association constant (K_a), enthalpy (ΔH), entropy (ΔS), and Gibbs free energy (ΔG) may be calculated. From this data set, hypotheses about the thermodynamic driving force, binding strength, mechanism, and favorability of the binding may be drawn.

In this study, we use ITC coupled with solid-state NMR (ssNMR) and potentiometric titrations to investigate the binding behavior MOFs with an organophosphorus probe molecule, ethylphosphonic acid (EPA). We chose this molecule since it mimics a CWA simulant hydrolysis product and has previously shown success with ITC to study MOF binding interactions.[42,43] Our library of MOFs contain metal nodes that span the spectrum of water exchange rates and Lewis acidity: Zr-NU-1000, Hf-NU-1000, Fe-MIL-100, Zn-MFU-4l, and Co-MFU-4l. Using ITC, we

constructed full thermodynamic binding profiles (ΔH, ΔG, ΔS, and K_a) for EPA with the selected MOFs. We then investigated the acidic properties of the nodes using ^{31}P magic angle spinning (MAS) ssNMR with adsorbed trimethylphosphine oxide (TMPO) and acid/base titrations to determine pK_a values of coordinated hydroxyl/water at the node. We found that not one factor alone (water exchange rate of aqua-ion complex, Lewis acidity of the node, pK_a at the node) is the sole driving force of the strength (K_a) or favorability (ΔH) of EPA binding in the MOFs studied here. Rather, we hypothesize that some combination, as well as the physical properties of the MOF and its node structure, all contribute to the thermodynamic trends observed for these materials. Most importantly, we further showcase ITC as a viable, powerful tool for measuring binding interactions in MOF systems, which has been relatively underexplored in this field.

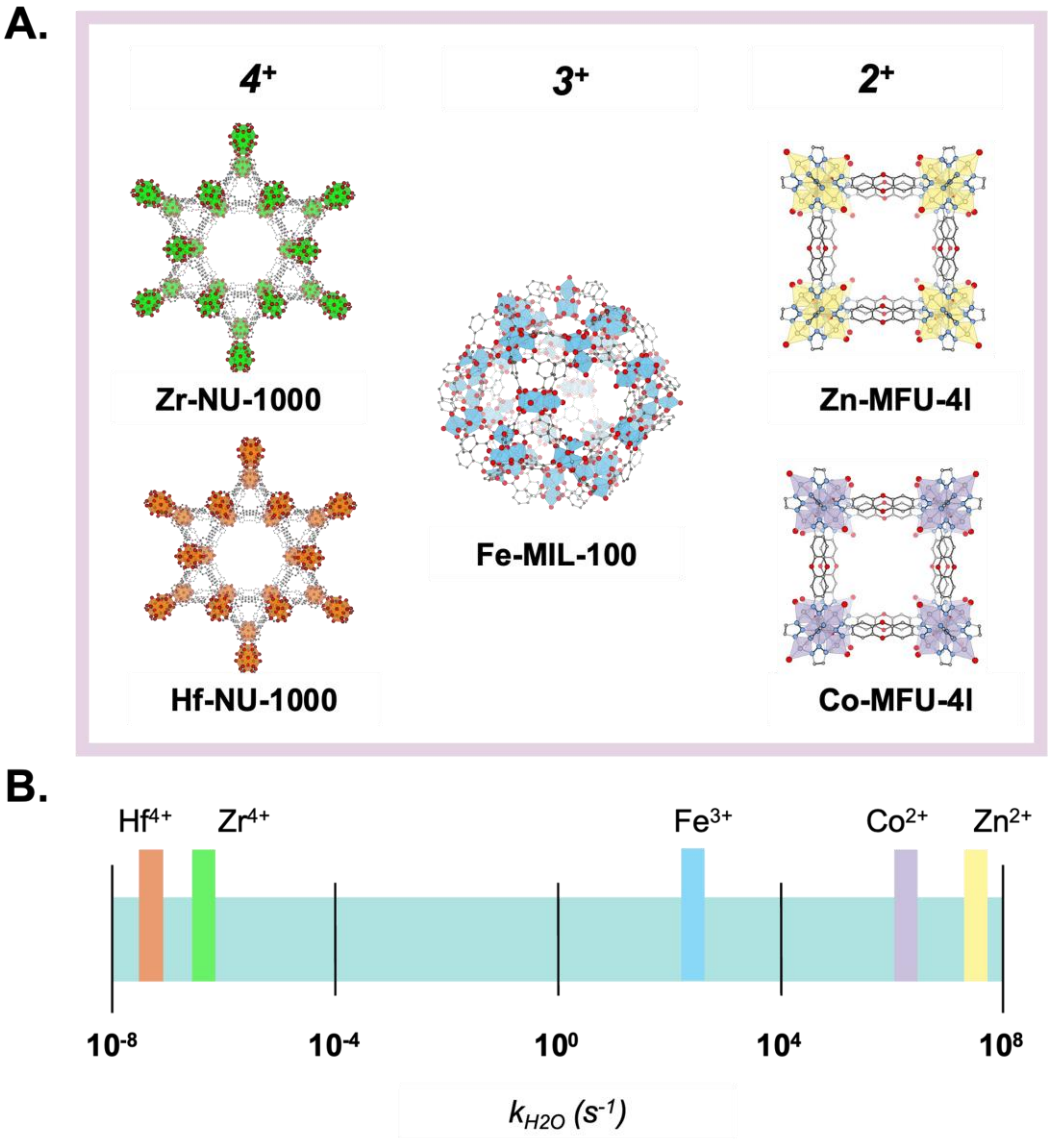

Figure 1. A) Crystal structures of the selected MOFs and B) approximate water exchange rate values for water-aqua complexes of metal ions.

MATERIALS AND METHODS:

Materials

All materials, unless otherwise specified, were purchased and used as received.

Zirconyl chloride octahydrate ($ZrOCl_2{\cdot}8H_2O$), hafnium(IV) oxychloride octahydrate ($HfOCl_2{\cdot}8H_2O$), zinc(II) chloride ($ZnCl_2$), anhydrous cobalt chloride ($CoCl_2$), iron(III) chloride

hexahydrate ($FeCl_3 \cdot 6H_2O$), benzene-1,3,5-tricarboxylic acid (BTC), nitric acid (HNO_3), sodium nitrate ($NaNO_3$) trifluoroacetic acid (TFA), benzoic acid (BA), 4-aminobenzoic acid, Bis-Tris buffer (0.2 M), and MilliQ water were purchased from Sigma Aldrich (St. Louis, MO). *N,N*-dimethyl formamide (DMF), acetone, ethanol, dichloro methane, sulfuric acid (H_2SO_4), hydrochloric acid (HCl), potassium hydroxide (KOH), and Decon™ Contrad™ 70 were purchased from Fisher (Fisher Scientific, Hampton, NH).

Instrumentation

N_2 isotherms were performed on a Micromeritics ASAP2420 porosity and surface area analyzer (Micromeritics, Norcross, GA) at 77 K. Surface areas were calculated using a BET model. Powder X-ray diffraction (PXRD) measurements were taken on a STOE-STADI-P (IMSERC-Northwestern University) run on pure CuKα1 radiation (λ = 1.54056 Å). Samples were prepared by packing dry powder into a PXRD mask. Data was collected from 0-40 º 2θ with a step size of 4.005 and time/PSD step set to 25 seconds. Scanning electron microscopy (SEM) images were collected using a JEOL JSM- 7900FLV scanning electron microscope. Powder samples were loaded on carbon tape and blown with compressed air. Prior to imaging, the samples were coated with 18 nm of osmium oxide using an SPF Osmium Coater (NUANCE Center-Northwestern University). Inductively coupled plasma-optical electron spectroscopy (ICP-OES) data were obtained using a Thermo iCAP 7600 ICP Spectrometer. Standards of Zr and Co (0.2 ppm–9.5 ppm) were prepared via serial dilution in MilliQ water and 2% nitric acid. MOF samples were digested via microwave digestion prior to analysis (QBIC-Northwestern University). X-ray photoelectron spectroscopy measurements were taken on a NEXSA G2 XPS (KECK-II/NUANCE-Northwestern University) using Al Kα radiation (hν = 1486.6 eV) equipped with an electron flood gun. Samples were prepared by mounting dry powder onto a flat sample holder with

copper tape. Collected data was analyzed using Thermo Scientific Advantage Data System software and peaks were referenced to adventitious C1s (284.8 eV).

Methods

Isothermal titration calorimetry (ITC): ITC was performed on a TA Instruments Affinity ITC (Waters, TA Instruments, Newcastle DE). The instrument syringe and sample cell were rinsed several times with 10% Contrad70, deionized water, MilliQ water, and 10 mM Bis-Tris buffer. The reference cell was loaded with 350 µL of MilliQ water. The sample cell was filled with 350 µL of 1 mM MOF in 10 mM Bis-Tris buffer. The 5 mM ethylphosphonic acid solution in 10 mM Bis-Tris buffer was titrated with 50 injections of 2 µL. The stir rate was set to 125 rpm and the equilibration time was 300 seconds. All titrations were performed at room temperature (25 ºC).

Potentiometric titrations: Acid-base titrations were obtained using a Metrohm Titrando 905 equipped with Dosino 800 20 mL and 10 mL dosing units. Calibration was performed with commercial pH buffers 2.00, 4.00, 7.00, and 9.00 (Metrohm). Samples were prepared by suspending about 40 mg of MOF in 50 mL of 0.01 M $NaNO_3$. This was left to equilibrate by stirring covered overnight at room temperature. The pH of the solution was adjusted to 3 by adding a few drops of 1 M HCl. The samples were titrated with 0.1 M NaOH at a rate of 0.1 mL/min until the pH reached 11.

Solid state ^{31}P NMR with Magic Angle Spinning: ssNMR data were collected on a Bruker Avance III 400 MHz Spectrometer equipped with a 4mm HX probe and sample data was acquired using TopSpin by Bruker. Samples were packed into a 4mm ZrO_2 rotor and sealed with

a Kel-F cap from Bruker. Spectra were collected at room temperature with a spin rate of 10 KHz and scan number of 100-200.

MOF synthesis

Preparation of Zr-NU-1000: Zr-NU-1000 was synthesized according to the literature procedure.[44] $ZrOC_{l2}\cdot 8H_2O$ (98 mg, 0.30 mmol) and benzoic acid (2 g, 16.38 mmol) were mixed in 8 mL of DMF in an 8-dram vial and dissolved by sonication. The clear solution was incubated in an oven at 100 °C for 1 h. After cooling down to room temperature, 1,3,6,8-tetrakis(p-benzoate)pyrene (H_4TBAPy) (40 mg, 0.06 mmol) and trifluoroacetic acid (TFA) (40 μL, 0.52 mmol) were added and sonicated for 10 min. The yellow suspension was heated by convection at 100 °C for 18 h. After cooling down to room temperature, yellow polycrystalline material was isolated by centrifugation (5 min, 7500 rpm) and washed three times with 15 mL of DMF. An HCl washing step was performed as follows to remove coordinated modulator from the node. The resulting yellow powder was suspended in 12 mL DMF and 0.5 mL of 8 M aqueous HCl was added. This mixture was heated in an oven at 100 °C for 18 h. After cooling to room temperature, the powder was isolated by centrifugation and washed three times with 15 mL of dimethylformamide (DMF) and three times with 15 mL acetone and soaked in acetone for additional 16 h. Zr-NU-1000 powder was collected by centrifugation, dried in a vacuum oven at 80 °C for 1 h, and then activated on a Micromeritics ASAP2420 instrument.

Preparation of Hf-NU-1000: Hf-NU-1000 was synthesized according to the literature procedure with slight modification.[45] First, $HfOCl_2\cdot 8H_2O$ (375 mg, 0.92 mmol) was dissolved in 8 mL of DMF in a 100 mL bottle. In a separate, 6-dram vial, H_4TBAPy (120 mg, 0.176 mmol) was

combined with 4-aminobenzoic acid (6.75 g, 49.2 mmol) and both were dissolved in 9 mL of DMF. Both solutions were incubated for 1 h at 100 ºC. Once cooled, the solutions were combined and 40 µL of TFA was added. After sonication for 5 minutes, the clear solution was heated at 120 ºC for 18 h. After cooling to room temperature, the yellow solid was collected *via* centrifugation, washed three times with DMF, and suspended in a solution of 26 mL DMF and 1.5 mL 8 M HCl. This solution was placed in an oven at 100 ºC overnight. The resulting powder was isolated by centrifugation and washed three times with 20 mL of DMF, three times with 20 mL acetone, and soaked in acetone for additional 16 h. Hf-NU-1000 powder was collected by centrifugation (8000 rpm, 3 minutes), dried in a vacuum oven at 80 °C for 1 h, and then activated on a Micromeritics ASAP2420 instrument.

Preparation of Zn-MFU-4l: Zn-MFU-4l was synthesized according to the literature procedure.[46] In a typical synthesis, 100 mg of 1H,7H-[1,4]Dioxino[2,3-F:5,6-F']Bisbenzotriazole (BTDD, 0.36 mmol) was added to 1.0 g of $ZnCl_2$ (7.3 mmol) in a 100 mL scintillation bottle. To this, 60 mL of DMF was added, and the solution was sonicated for several minutes. The brown solution was heated for 18 hours at 140 ºC in a synthesis oven and cooled down to room temperature. The light brown solid was collected by centrifugation (8000 rpm, 3 minutes), then washed three times with 20 mL DMF, three times with 20 mL methanol, and three times with 20 mL DCM. The solid was dried in a vacuum oven at 80 ºC for two hours and activated at 180 ºC under dynamic vacuum overnight.

Preparation of Co-MFU-4l: Co-MFU-4l was synthesized according to previously published procedures with slight modification.[47] 100 mg of Zn-MFU-4l (0.08 mmol) was added to a solution

of anhydrous $CoCl_2$ (0.5 g, 2.1 mmol) dissolved in 16 mL of DMF in an 8-dram vial. The solution was heated at 140 ºC for 20 h in an oven. The blue-green solid was collected via centrifugation (8000 rpm, 3 minutes) and washed three times with 20 mL DMF, three times with 20 mL methanol, and three times with 20 mL DCM. The solid was dried in a vacuum oven at 80 ºC for 2 h and activated at 180 ºC under dynamic vacuum overnight. ICP-OES confirmed 3.9 Co^{2+} per node.

Preparation of Fe-MIL-100: Fe-MIL-100 was synthesized according to literature procedure with slight modification.[48] In a jar, $FeCl_3 \cdot 6H_2O$ (2.0 g, 7.4 mmol), BTC (1.055 g, 5.0 mmol), 4.4 mL of HNO_3, and 22.1 mL of water were combined and sonicated for several minutes. This solution was divided equally between 4 different Parr **v**essels and heated overnight at 150 ºC. The orange solid was collected by centrifugation (8000 rpm, 3 minutes) and washed three times with 20 mL water and three times with 20 mL of ethanol. The solid was left soaking in ethanol overnight before it was collected, dried in a vacuum oven at 80 ºC for 2 h and activated at 120 ºC under dynamic vacuum overnight.

Preparation of Al-NU-2000: NU-2000 was synthesized according to the literature procedure.[49] In a Parr vessel, bicylo[2.2.2]octane-1,4-dicarboxylic acid (137 mg, 0.69 mmol), aluminum chloride hexahydrate (335 mg, 1.39 mmol), and water (3 mL) were added. The mixture was heated at 200 ºC in a convection oven, cooled to room temperature, and isolated *via* centrifugation. The collected solid was washed three times with water, three times with DMF at 120 ºC, and three times with acetone and allowed to soak in acetone overnight. The sample was then dried in a vacuum oven at 80 ºC before thermal activation under dynamic vacuum at 300 ºC.

RESULTS:

MOF selection

Our study began by synthesizing a variety of different MOFs whose nodes contain metals in the 4^+, 3^+, and 2^+ oxidation states, spanning a wide range of water exchange rates and Lewis acidities. In the 4^+ category, we chose Zr- and Hf-NU-1000, two well-studied, isostructural pyrene-based MOFs with *csq* topology. The hexanuclear, 8-connected nodes include bridging oxo groups and coordinated water or hydroxyl. Since both Zr^{4+} and Hf^{4+} have high charge densities, are strongly polarizing, and display hard acid characteristics, their metal-aqua complexes exhibit slow water exchange rates predicted to be in the range of 10^{-8} – 10^{-6} s^{-1}.[50] On the other hand, they are highly Lewis acidic and thus are used as potent catalysts for a variety of chemical transformations.[51–54] At the other end of the spectrum, we elected to investigate Zn- and Co-MFU-4l, whose nodes include the 2^+ oxidation state transition metals. These two azolate MOFs crystallize in the cubic *pcu* topology and contain pentanuclear Kuratowski-type nodes with a central octahedral Zn^{2+} and four peripheral tetrahedral Zn^{2+} or Co^{2+} ions coordinated to three nitrogen atoms and one charge-balancing ion (chloride or hydroxyl). Notably, the *de novo* synthesis has only been reported for Zn-MFU-4l, so the Co analogue was accessed *via* post-synthetic transmetallation, with a Co:Zn ratio of 3.9:1.1, which is expected since the central Zn cannot be exchanged. Both Zn^{2+} and Co^{2+} have lower relative charge densities and are generally considered to be softer or borderline acids. Therefore, the water exchange rates of their metal-aqua ions are much faster, in the range of 10^6 – 10^8 s^{-1}. Finally, to cover the intermediary, we selected Fe-MIL-100, a *mtn* zeolite-like MOF with trivalent metal nodes containing ions in the 3^+ oxidation state. Fe-MIL-100 crystalizes with tritopic trimesic acid linkers resulting in large cages of 25 and 29 Å diameters.[55]

Characterization data for each MOF, including nitrogen adsorption/desorption isotherms, powder X-ray diffraction (PXRD) patterns, and scanning electron microscopy (SEM) images can be found in the supplemental information (Figure S1 – Figure S11).

Buffer Stability

Overall, each MOF was selected with careful consideration of stability in aqueous buffer conditions and available open metal sites for guest coordination. NU-1000 and MFU-4l have been previously investigated with confirmed water stability.[42,43] As for Fe-MIL-100, we carried out stability tests to ensure it maintains porosity and crystallinity in the presence of water and buffer (Figure S13). We suspended about 40 mg of MOF in about 50 mL of the chosen buffer for the ITC experiments, 10 mM bis(2-hydroxyethyl)aminotris(hydroxymethyl)methane (Bis-Tris) buffer with pH 6.4, for 3 hours. The solid was collected, washed three times with water and three times with ethanol, dried in a vacuum oven at 85 ºC, and activated at 120 ºC overnight. Comparison of nitrogen adsorption/desorption isotherms and PXRD patterns before and after exposure to the buffer confirms that the MOFs retain their porosity and crystallinity in buffer conditions.

Aside from MOF stability, another important control for ITC experiments is to ensure that the buffer interacts minimally with the MOFs. This maintains that the heat recorded from an ITC experiment reflects the analyte interaction with the MOF rather than buffer or dilution effects. For each of these controls, 350 μL of a 1 mM MOF solution in 10 mM Bis-Tris buffer was loaded into the sample cell. To the syringe was added 10 mM Bis-Tris buffer, which was titrated in 2 μL injections with 300 s equilibration time for 50 injections. For each MOF, small, equal peaks were observed in the thermogram and displayed minimal enthalpy contributions, confirming that the buffer has minimal interaction with the MOFs (Figure S15 – Figure S19). Similarly, we wanted to ensure the analyte, ethylphosphonic acid (EPA), doesn't interact significantly with the buffer. To

this end, we titrated 5 mM EPA into a 350 μL solution of 10 mM Bis-Tris, which resulted in small, insignificant peaks in the thermogram with minimal enthalpy change (Figure S14).

ITC Binding Experiments

After we confirmed that the buffer does not interact with the MOFs nor EPA, we began our ITC studies. For the general set-up, a 1 mM MOF solution was prepared in 10 mM Bis-Tris buffer. Solutions were sonicated for several minutes to disperse the MOF and ensure an even suspension. The pH was adjusted to 6.4 with several drops of KOH. Next, 350 μL of the MOF solution was added to the cleaned and rinsed sample cell. The syringe was loaded 150 μL of 5 mM EPA in 10 mM Bis-Tris with pH 6.4. After an equilibration period, EPA was titrated into the MOF with 2 μL injections every 300 s for a total of 50 injections. Titrations were collected in triplicate for each MOF.

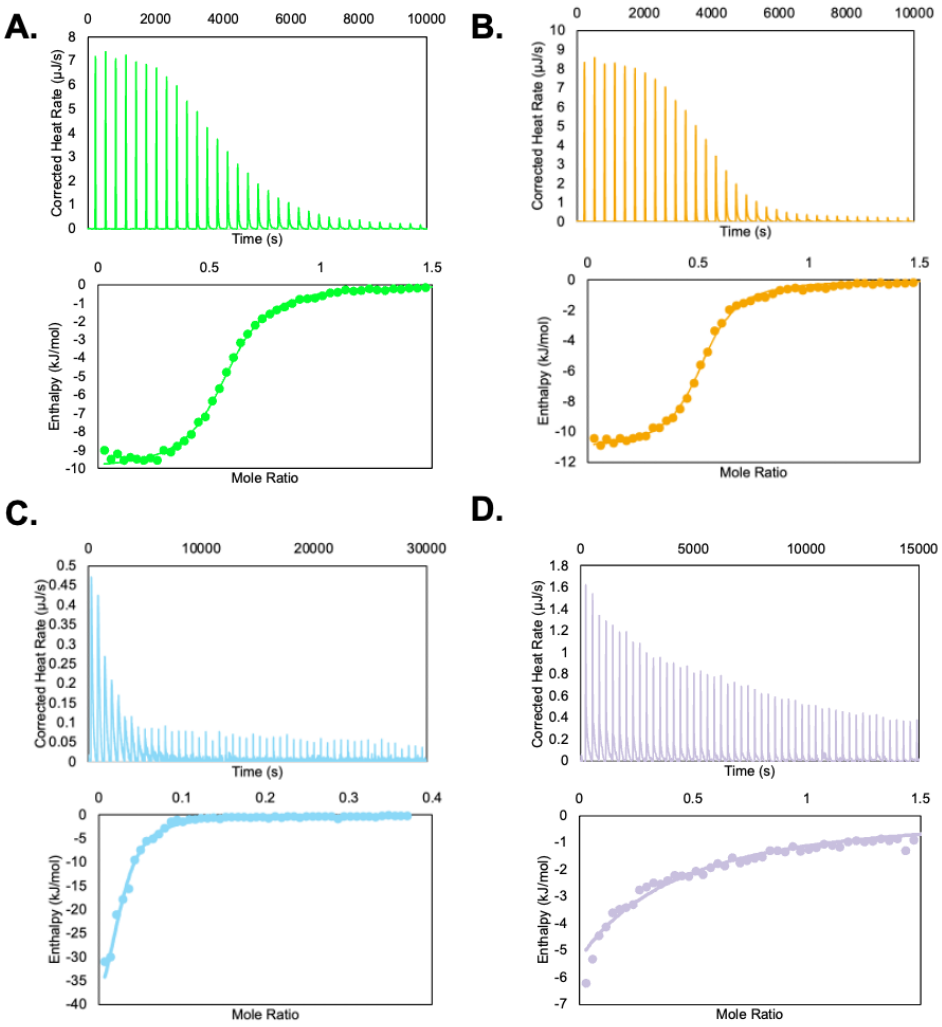

Figure 2. Representative ITC thermogram (top) and resulting binding curve (bottom) from the titration of 5 mM EPA into 1 mM A) Zr-NU-1000, B) Hf-NU-1000, C) Fe-MIL-100, and D) Co-MFU-4l. All solutions were prepared in 10 mM Bis-Tris buffer, pH 6.4.

The thermograms of the two NU-1000 MOFs displayed large, exothermic peaks that resulted in substantial enthalpy changes and a large, negative Gibbs free energy change (Figure 2A – B). Zr-NU-1000 measured a ΔH of -10.16 (±0.68) kJ/mol and a strong K_a of 6.37 (±3.0) × 10^4 M^{-1}. Hf-NU-1000 displayed similarly strong binding with EPA, measuring an enthalpy change of ΔH = -12.14 (±1.5) kJ/mol and a K_a of 5.8 (±2.0) × 10^4 M^{-1}. The large positive entropy changes in terms of -TΔS (-17.08 ±1.78 kJ/mol for Zr-NU-1000 and -14.94 ± 2.4 kJ/mol for Hf-NU-1000)

observed in both cases points to a possible rearrangement of water molecules at the node that increased the overall entropy of the system. In the case of the divalent MFU-4l MOFs, we see peaks in the thermograms with roughly a quarter of the intensity as the tetravalent NU-1000 materials. The weaker, less favorable binding is measured with smaller ΔH magnitudes of -4.38 (±0.36) and -4.47 (±0.98) kJ/mol for Zn- and Co-MFU-4l, respectively (Figure 2D, Figure S20). The negative enthalpies calculated from the binding curves suggest an exothermic pathway for the interaction, and negative ΔG values, though smaller in magnitude compared to the NU-1000 MOFs, suggest the binding is spontaneous. In the case of the trivalent MOF, Fe-MIL-100 surprisingly recorded the highest enthalpy change of ΔH = -26.56 (±3.85), surpassing even that of Hf and Zr-NU-1000 (Figure 2C). For this case, the injection volume was reduced to 0.5 μL to deconvolute the broad peak of the first injection seen with a 2 μL injection volume. The binding association constant of Fe-MIL-100 measured 7.92 (±3.0) × 10^4 M^{-1}, on par with the tetravalent MOFs. Additionally, the entropy change from EPA interaction with Fe-MIL-100 is negligible, suggesting that the driving force for the interaction is enthalpy-driven. All the materials, however, exhibit large negative Gibbs free energy indicative of a favorable, spontaneous interaction. Thermodynamic parameters of the five MOFs are compared in Figure 3.

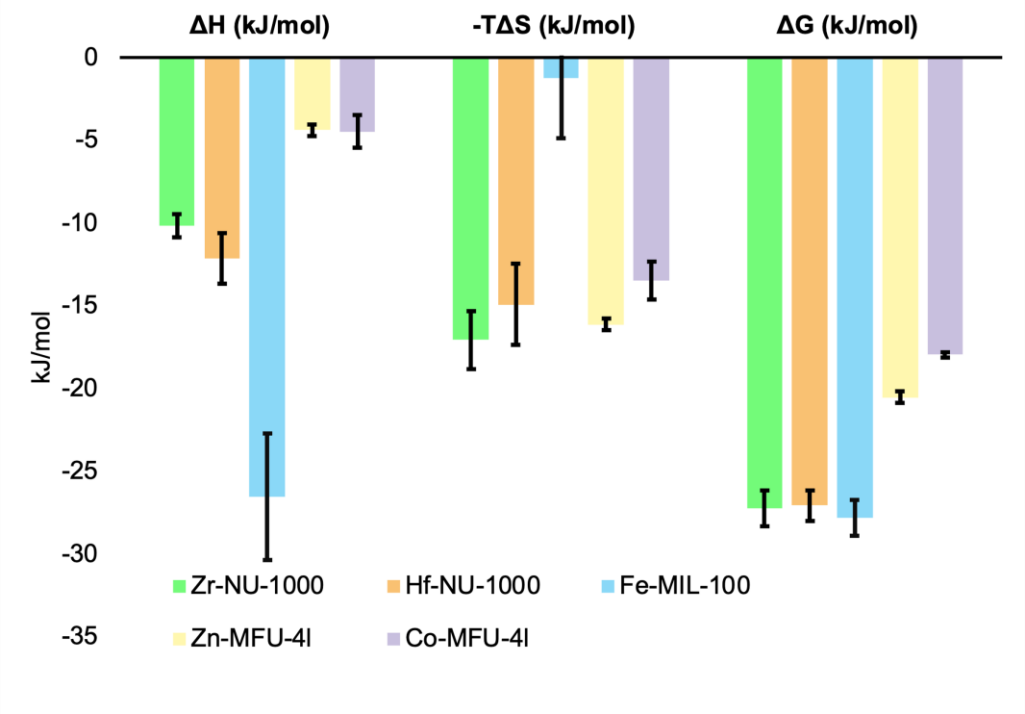

Figure 3. Thermodynamic parameters for EPA binding in selected MOFs calculated from a single-site binding model. Error bars represent standard deviation of three trials.

Potentiometric Titrations

One way to probe the Lewis Acidity of metal sites within MOFs is to perform potentiometric titrations to determine the pK_a of protons present on the node. Since the pK_a values for Zr-NU-1000, Zn-MFU-4l, and Co-MFU-4l have been reported,[47,56] we took measurements for Hf-NU-1000 and Fe-MIL-100. The reported pK_{a1} for Zr-NU-1000, 3.59, matches well with the measured pK_{a1} of Hf-NU-1000 reported here as 3.31 (Figure 4A). These low values hint at acidic protons on the coordinated bridging hydroxyl, suggesting highly Lewis acidic metal sites. On the other hand, the reported pK_{a1} values for coordinated water on the nodes of Zn- and Co-MFU-4l are 7.7 and 8.5, respectively. The expected lower values are indicative of the weaker acidity of the divalent metals compared to the tetravalent Hf and Zr. From the titration curve of Fe-MIL-100, a pK_{a1} of 3.1, pK_{a2} of 6.33, pK_{a3} of 7.20, and pK_{a4} of 8.35 were measured, indicating a wide range of

acidic sites (Figure 4B). Of note is the low pK_{a1} value that rivals those of Hf- and Zr-NU-1000, pointing to the possibility of a local structural motif with enhanced Lewis acidity.

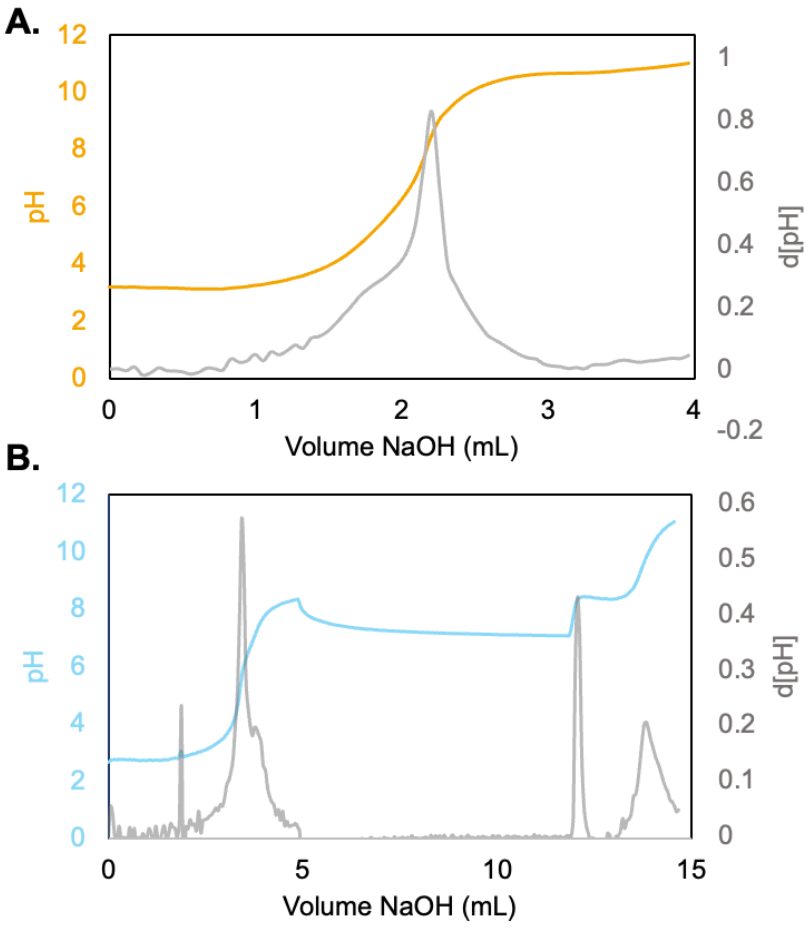

Figure 4. Potentiometric titration curves for A) Hf-NU-1000 and B) Fe-MIL-100 in 10 mM $NaNO_3$. Gray traces are the first derivative which indicate the equivalence points.

Solid-State ^{31}P-NMR

To get a better understanding of the acid sites in these MOFs, we ran solid-state ^{31}P MAS NMR (ssNMR) experiments with trimethyl phosphine oxide (TMPO). Monitoring peak shifts of adsorbed phosphines is a well-studied strategy to gain insight into local structure and acidic sites on solid catalysts, including porous materials.[57–60] In a typical set-up, each material was treated

with 0.2 M TMPO in DCM under an inert argon atmosphere for 18 hours. The excess solvent and uncoordinated TMPO was removed *via* vacuum.

Similar peak positions in the range of δ 20 – 70 ppm were observed for all materials, with spinning sidebands around δ -10 and 110 ppm. The main peak from the Hf- and Zr-NU-1000 samples appeared at δ 52.8 and 52.0 ppm, respectively. The less Lewis acidic Zn-MFU-4l expectedly has an upshifted peak centered at δ 48.7 ppm. The signal for Fe-MIL-100 fell in the middle of these two ranges at 51.3 ppm, which is in line with the predicted Lewis acidity trend. The spectra are shown in Figure 5, except for Co-MFU-4l, whose paramagnetic nature prevented the collection of sharp peaks that could be deconvoluted from spinning sidebands (Figure S21).

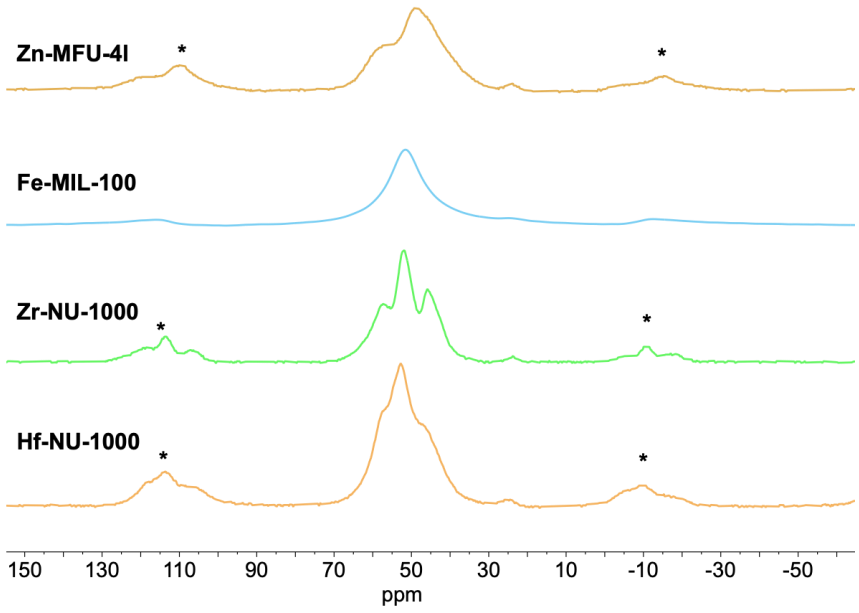

Figure 5. Solid-state ^{31}P MAS NMR spectra for TMPO-treated MOFs. Spinning sidebands are denoted with (*).

DISCUSSION

Water exchange rate and Lewis acidity

The individual metals comprising the nodes of the selected MOFs have a wide range of properties, including Lewis acidity and water exchange rates of their metal-aqua complexes. Generally, highly Lewis acidic metals, key for many catalytic transformations, inversely exhibit slow k_{H2O}, which can negatively impact turnover. From the series of MOFs studied here, Zr^{4+} and Hf^{4+} are the most Lewis acidic and exhibit the slowest k_{H2O} in the range of 10^{-8} – 10^{-6} s^{-1}. On the other end of the spectrum, while exhibiting some Lewis acidic character, Zn^{2+} and Co^{2+} have much faster k_{H2O} values in the range of 10^{6} – 10^{8} s^{-1}. The trivalent metal falls in the middle of this spectrum, with Fe^{3+} exhibiting an intermediate exchange rate of 1.6×10^{2} s^{-1}. If we expected the enthalpy change of binding between EPA and the MOFs calculated from ITC experiments to correlate inversely with k_{H2O}, we would see $Hf^{4+} \sim Zr^{4+} > Fe^{3+} > Co^{2+} > Zn^{2+}$. However, the trend for enthalpy change from the ITC data observed was $Fe^{3+} > Hf^{4+} \sim Zr^{4+} > Zn^{2+} \sim Co^{2+}$. This hints to the influence of other factors impacting the EPA binding in the studied MOFs pertaining to their structure, chemical composition, or physical properties.

The water exchange rate and Lewis acidity of metal ions within MOF nodes is likely not a 1:1 comparison with their corresponding isolated metal-aqua complexes. For one, most of the coordinating moieties on the MOF node are functional groups from the linker rather than water. While water is present on the node to varying degrees in these MOFs, the strength of its binding is influenced by the electronic properties of the node which are tuned by the identity of coordinating groups, number of coordinating groups, and proximity to neighboring metal ions. Additionally, surface defects, which are not extensively characterized here, alter the local structure of the material, perhaps inducing the formation of microenvironments with different material properties than the bulk crystallite and/or powder.

Metal node acidity

The acidity of the nodes within the MOFs of the chosen series likely impacts the observed binding with the organophosphonate probe. Both potentiometric titrations and ssNMR are viable techniques to gain insight into the metal acidity of MOF nodes. Acid-base titrations reveal pK_a values of protons present in the nodes to evaluate their Brønsted acidity and distinguish between unique sites. Lower pK_a values of protons from coordinated water or hydroxyl groups correlate to stronger Lewis acidic metals.[56] In this vein, from reported and observed pK_{a1} values, the trend was found to be $Fe^{3+} > Hf^{4+} > Zr^{4+} > Zn^{2+} > Co^{2+}$. This finding contradicts established Lewis acidity trends of transition metals which place Fe^{3+} between the tetra and divalent metals. The surprisingly low pK_a from the titration with Fe-MIL-100 hints at the presence of structural or secondary effects within Fe-MIL-100 that tune the acidic properties of the node. This trend, however, matches well with both enthalpy changes and binding association constants for EPA interaction with the MOFs. From ssNMR spectra, the peak shifts do follow the expected Lewis acidity trend. The detection of more acidic sites on Fe-MIL-100 than NU-1000 seen in acid/base titrations but not in ssNMR may indicate that the aqueous environment plays a role in the thermodynamics of EPA binding—while potentiometric titrations and ITC were carried out in aqueous buffers, ssNMR samples were prepared with activated samples in dry solvent under an inert Ar atmosphere.

Inorganic node properties

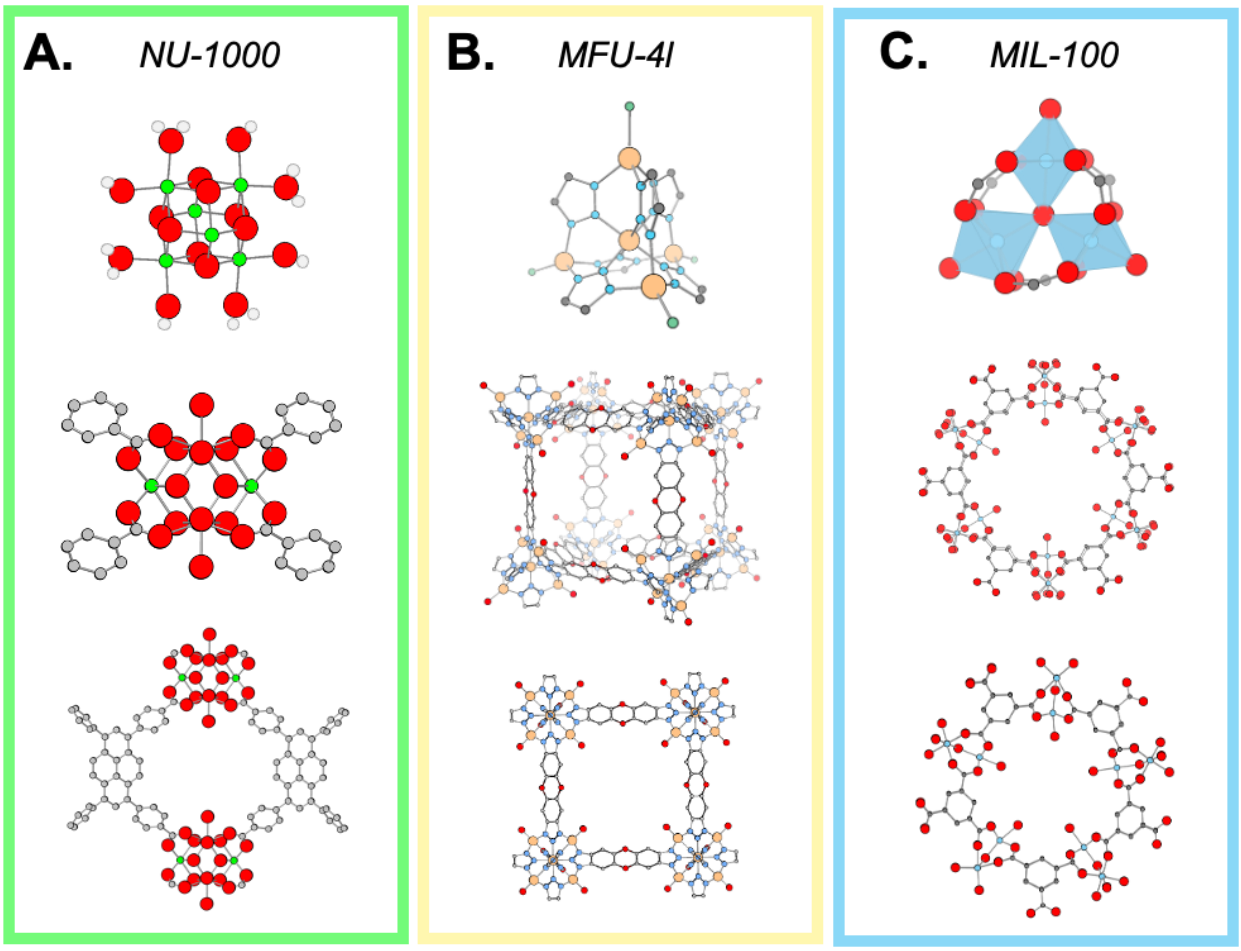

Figure 6. Inorganic nodes and pore structures from crystal structures of A) Zr/Hf-NU-1000, B) Zn/Co-MFU-4l, and C) Fe-MIL-100. Color code: O (red), Fe (blue), C (gray), Zn (yellow), N (teal). H omitted for clarity

Perhaps most important to understanding the strength of organophosphorus binding and acidity is the composition and geometry of the node. The availability of open metal sites, or the presence of labile water or hydroxide, is crucial for the binding of guest molecules to measure the enthalpy and binding strength of the interaction. It is hypothesized that in this system, the phosphonate oxygen from the P=O bond replaces coordinated water and binds to the node during ITC experiments (Figure 7). Zr- and Hf-NU-1000 contain hexanuclear nodes with both labile water and charge-balancing hydroxyl groups. Each metal is open to binding, positively contributing to

the large enthalpy change observed from ITC. Zn- and Co-MFU-4l have pentavalent nodes; however, only the four tetrahedrally coordinated peripheral metals have a labile counterion that can be replaced to bind a guest molecule. Here, the weaker acidity of the Zn and Co ions compared to that of Zr and Hf, in combination with the fewer accessible coordination sites per node, explains the differences in enthalpy changes and binding association constants from EPA adsorption. Fe-MIL-100 contains trivalent nodes with three labile water or hydroxyl groups. The iron MOF, which has the fewest coordinating sites per node but the largest enthalpy change upon phosphonate binding, reflects inherent features that contribute to its strong binding. Here, the node acidity, estimated from observed pK_a, is likely the driving force for the strong interaction with the organophosphonate. One possible contribution is the redox activity of trivalent Fe ($Fe^{3+} + e^- \rightleftarrows Fe^{2+}$). A lower oxidation state of Fe in the node would necessitate more water ligands coordinated to the node than hydroxyl groups to properly charge balance, which are easier to replace than the more strongly coordinated anions. This availability of open metal sites as a crucial factor for detecting binding thermodynamics from ITC is further exemplified by a study with Al-NU-2000, a MOF with a chain-based node containing no open coordination sites. Titration with EPA resulted in no noticeable heat changes, indicating minimal interaction with the framework due to a lack of accessibility to the node. These data suggest that metal node identity and their properties, including water exchange rate, acidity, and availability of open metal sites, all contribute to the favorability and strength of organophosphorus binding. For coordination complexes, values like Lewis acidity and water exchange rates are usually enough to predict certain properties. It becomes much more complicated in MOF systems due to the structural rigidity, steric strains, and surface effects that tune the material properties.

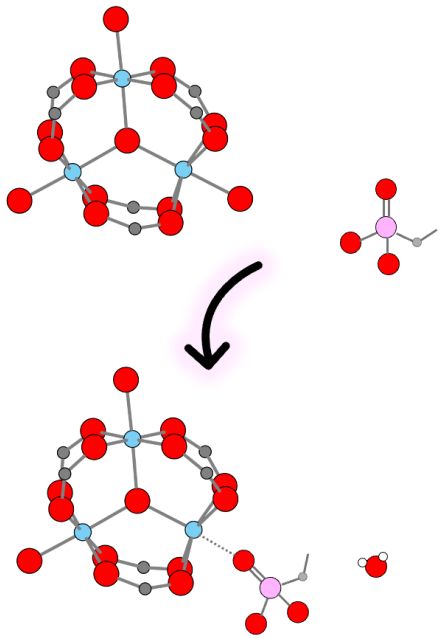

Figure 7. Schematic of EPA replacing a water molecule at the node of Fe-MIL-100 during a binding interaction. Color code: O (red), Fe (blue), C (gray), P (pink). H omitted for clarity.

CONCLUSION

In conclusion, this study explored the binding interaction of a series of MOFs with an organophosphorus probe, EPA. The library of MOFs chosen (Hf-NU-1000, Zr-NU-1000, Fe-MIL-100, Zn-MFU-4l, Co-MFU-4l) contain a variety of metals in oxidation states ranging from 2^+ to 4^+. The individual metals span a large range of Lewis acidities and water exchange rates of their metal-aqua complexes. To better understand how these inorganic properties influence organophosphorus binding in MOF systems, we used isothermal titration calorimetry to measure the binding thermodynamics between the MOFs and EPA. While we observed strong binding thermodynamics for the tetravalent Hf and Zr MOFs and weaker binding in the divalent azolate materials, Fe-MIL-100 surprisingly recorded the strongest phosphonate binding, with over double the enthalpy change compared to the other materials. We coupled these ITC experiments with potentiometric titrations as well as solid-state NMR experiments to investigate how the acidities

of the metal node may have impacted this observed organophosphorus binding. We found that while Fe^{3+} alone is known as a weaker Lewis acid than the tetravalent ions, the Fe-MIL-100 studied here may have some local structural features with enhanced acidic properties. For example, acid/base titrations measured a pK_a of 3.1, slightly lower than Hf- and Zr-NU-1000. Ultimately, while metal properties can provide insights into MOF behavior for certain applications, the material's overall properties are shaped by a complex interplay of factors. We suggest a combination of node structure, Lewis acidities, and accessible open binding sites influences the thermodynamics of organophosphorus binding in MOFs. A more complete understanding of the binding thermodynamics of adsorbates in the context of materials properties will help inform the design of more effective MOFs for applications such as catalysis and selective adsorption. Most noteworthy is the continued development of ITC as a viable technique to measure MOF/adsorbate interactions, which has been relatively underexplored in this field.

CITATIONS

(1) Furukawa, H.; Cordova, K. E.; O'Keeffe, M.; Yaghi, O. M. The Chemistry and Applications of Metal-Organic Frameworks. *Science* **2013**, *341* (6149), 1230444. https://doi.org/10.1126/science.1230444.

(2) Koschnick, C.; Terban, M. W.; Frison, R.; Etter, M.; Böhm, F. A.; Proserpio, D. M.; Krause, S.; Dinnebier, R. E.; Canossa, S.; Lotsch, B. V. Unlocking New Topologies in Zr-Based Metal–Organic Frameworks by Combining Linker Flexibility and Building Block Disorder. *J. Am. Chem. Soc.* **2023**, *145* (18), 10051–10060. https://doi.org/10.1021/jacs.2c13731.

(3) Glasby, L. T.; Cordiner, J. L.; Cole, J. C.; Moghadam, P. Z. Topological Characterization of Metal–Organic Frameworks: A Perspective. *Chem. Mater.* **2024**, *36* (19), 9013–9030. https://doi.org/10.1021/acs.chemmater.4c00762.

(4) Li, P.; Moon, S.-Y.; Guelta, M. A.; Lin, L.; Gómez-Gualdrón, D. A.; Snurr, R. Q.; Harvey, S. P.; Hupp, J. T.; Farha, O. K. Nanosizing a Metal–Organic Framework Enzyme Carrier for Accelerating Nerve Agent Hydrolysis. *ACS Nano* **2016**, *10* (10), 9174–9182. https://doi.org/10.1021/acsnano.6b04996.

(5) Eddaoudi, M.; Kim, J.; Rosi, N.; Vodak, D.; Wachter, J.; O'Keeffe, M.; Yaghi, O. M. Systematic Design of Pore Size and Functionality in Isoreticular MOFs and Their Application in Methane Storage. *Science* **2002**, *295* (5554), 469–472. https://doi.org/10.1126/science.1067208.

(6) Deng, H.; Grunder, S.; Cordova, K. E.; Valente, C.; Furukawa, H.; Hmadeh, M.; Gándara, F.; Whalley, A. C.; Liu, Z.; Asahina, S.; Kazumori, H.; O'Keeffe, M.; Terasaki, O.; Stoddart, J. F.; Yaghi, O. M. Large-Pore Apertures in a Series of Metal-Organic Frameworks. *Science* **2012**, *336* (6084), 1018–1023. https://doi.org/10.1126/science.1220131.

(7) Feng, L.; Day, G. S.; Wang, K.-Y.; Yuan, S.; Zhou, H.-C. Strategies for Pore Engineering in Zirconium Metal-Organic Frameworks. *Chem* **2020**, *6* (11), 2902–2923. https://doi.org/10.1016/j.chempr.2020.09.010.

(8) Flaig, R. W.; Osborn Popp, T. M.; Fracaroli, A. M.; Kapustin, E. A.; Kalmutzki, M. J.; Altamimi, R. M.; Fathieh, F.; Reimer, J. A.; Yaghi, O. M. The Chemistry of CO2 Capture in an Amine-Functionalized Metal–Organic Framework under Dry and Humid Conditions. *J. Am. Chem. Soc.* **2017**, *139* (35), 12125–12128. https://doi.org/10.1021/jacs.7b06382.

(9) Bose, S.; Sengupta, D.; D. Malliakas, C.; B. Idrees, K.; Xie, H.; Wang, X.; L. Barsoum, M.; M. Barker, N.; P. Dravid, V.; Islamoglu, T.; K. Farha, O. Suitability of a Diamine Functionalized Metal–Organic Framework for Direct Air Capture. *Chem. Sci.* **2023**, *14* (35), 9380–9388. https://doi.org/10.1039/D3SC02554C.

(10) S. Forgan, R. The Surface Chemistry of Metal–Organic Frameworks and Their Applications. *Dalton Trans.* **2019**, *48* (25), 9037–9042. https://doi.org/10.1039/C9DT01710K.

(11) DeSantis, D.; Mason, J. A.; James, B. D.; Houchins, C.; Long, J. R.; Veenstra, M. Techno-Economic Analysis of Metal–Organic Frameworks for Hydrogen and Natural Gas Storage. *Energy Fuels* **2017**, *31* (2), 2024–2032. https://doi.org/10.1021/acs.energyfuels.6b02510.

(12) Sengupta, D.; Melix, P.; Bose, S.; Duncan, J.; Wang, X.; Mian, M. R.; Kirlikovali, K. O.; Joodaki, F.; Islamoglu, T.; Yildirim, T.; Snurr, R. Q.; Farha, O. K. Air-Stable Cu(I) Metal–Organic Framework for Hydrogen Storage. *J. Am. Chem. Soc.* **2023**, *145* (37), 20492–20502. https://doi.org/10.1021/jacs.3c06393.

(13) Lin, J.-B.; Nguyen, T. T. T.; Vaidhyanathan, R.; Burner, J.; Taylor, J. M.; Durekova, H.; Akhtar, F.; Mah, R. K.; Ghaffari-Nik, O.; Marx, S.; Fylstra, N.; Iremonger, S. S.; Dawson, K. W.; Sarkar, P.; Hovington, P.; Rajendran, A.; Woo, T. K.; Shimizu, G. K. H. A Scalable Metal-Organic Framework as a Durable Physisorbent for Carbon Dioxide Capture. *Science* **2021**, *374* (6574), 1464–1469. https://doi.org/10.1126/science.abi7281.

(14) Britt, D.; Furukawa, H.; Wang, B.; Glover, T. G.; Yaghi, O. M. Highly Efficient Separation of Carbon Dioxide by a Metal-Organic Framework Replete with Open Metal Sites. *Proc. Natl. Acad. Sci.* **2009**, *106* (49), 20637–20640. https://doi.org/10.1073/pnas.0909718106.

(15) Bhatt, P. M.; Belmabkhout, Y.; Cadiau, A.; Adil, K.; Shekhah, O.; Shkurenko, A.; Barbour, L. J.; Eddaoudi, M. A Fine-Tuned Fluorinated MOF Addresses the Needs for Trace CO2 Removal and Air Capture Using Physisorption. *J. Am. Chem. Soc.* **2016**, *138* (29), 9301–9307. https://doi.org/10.1021/jacs.6b05345.

(16) Osterrieth, J. W. M.; Fairen-Jimenez, D. Metal–Organic Framework Composites for Theragnostics and Drug Delivery Applications. *Biotechnol. J.* **2021**, *16* (2), 2000005. https://doi.org/10.1002/biot.202000005.

(17) Horcajada, P.; Serre, C.; Maurin, G.; Ramsahye, N. A.; Balas, F.; Vallet-Regí, M.; Sebban, M.; Taulelle, F.; Férey, G. Flexible Porous Metal-Organic Frameworks for a Controlled Drug Delivery. *J. Am. Chem. Soc.* **2008**, *130* (21), 6774–6780. https://doi.org/10.1021/ja710973k.

(18) Ettlinger, R.; Sönksen, M.; Graf, M.; Moreno, N.; Denysenko, D.; Volkmer, D.; Kerl, K.; Bunzen, H. Metal–Organic Framework Nanoparticles for Arsenic Trioxide Drug Delivery. *J. Mater. Chem. B* **2018**, *6* (40), 6481–6489. https://doi.org/10.1039/C8TB01899E.

(19) Kreno, L. E.; Leong, K.; Farha, O. K.; Allendorf, M.; Van Duyne, R. P.; Hupp, J. T. Metal–Organic Framework Materials as Chemical Sensors. *Chem. Rev.* **2012**, *112* (2), 1105–1125. https://doi.org/10.1021/cr200324t.

(20) Raja Lakshmi, P.; Nanjan, P.; Kannan, S.; Shanmugaraju, S. Recent Advances in Luminescent Metal–Organic Frameworks (LMOFs) Based Fluorescent Sensors for Antibiotics. *Coord. Chem. Rev.* **2021**, *435*, 213793. https://doi.org/10.1016/j.ccr.2021.213793.

(21) Dolgopolova, E. A.; Rice, A. M.; Martin, C. R.; Shustova, N. B. Photochemistry and Photophysics of MOFs: Steps towards MOF-Based Sensing Enhancements. *Chem. Soc. Rev.* **2018**, *47* (13), 4710–4728. https://doi.org/10.1039/C7CS00861A.

(22) Xiao, D. J.; Bloch, E. D.; Mason, J. A.; Queen, W. L.; Hudson, M. R.; Planas, N.; Borycz, J.; Dzubak, A. L.; Verma, P.; Lee, K.; Bonino, F.; Crocellà, V.; Yano, J.; Bordiga, S.; Truhlar, D. G.; Gagliardi, L.; Brown, C. M.; Long, J. R. Oxidation of Ethane to Ethanol by N2O in a Metal–Organic Framework with Coordinatively Unsaturated Iron(II) Sites. *Nat. Chem.* **2014**, *6* (7), 590–595. https://doi.org/10.1038/nchem.1956.

(23) Wasson, M. C.; Buru, C. T.; Chen, Z.; Islamoglu, T.; Farha, O. K. Metal–Organic Frameworks: A Tunable Platform to Access Single-Site Heterogeneous Catalysts. *Appl. Catal. Gen.* **2019**, *586*, 117214. https://doi.org/10.1016/j.apcata.2019.117214.

(24) Lee, J.; Farha, O. K.; Roberts, J.; Scheidt, K. A.; Nguyen, S. T.; Hupp, J. T. Metal–Organic Framework Materials as Catalysts. *Chem. Soc. Rev.* **2009**, *38* (5), 1450–1459. https://doi.org/10.1039/B807080F.

(25) Kirlikovali, K. O.; Chen, Z.; Islamoglu, T.; Hupp, J. T.; Farha, O. K. Zirconium-Based Metal–Organic Frameworks for the Catalytic Hydrolysis of Organophosphorus Nerve Agents. *ACS Appl. Mater. Interfaces* **2020**, *12* (13), 14702–14720. https://doi.org/10.1021/acsami.9b20154.

(26) Moon, S.-Y.; Liu, Y.; Hupp, J. T.; Farha, O. K. Instantaneous Hydrolysis of Nerve-Agent Simulants with a Six-Connected Zirconium-Based Metal–Organic Framework. *Angew. Chem. Int. Ed.* **2015**, *54* (23), 6795–6799. https://doi.org/10.1002/anie.201502155.

(27) Chen, Z.; Islamoglu, T.; Farha, O. K. Toward Base Heterogenization: A Zirconium Metal–Organic Framework/Dendrimer or Polymer Mixture for Rapid Hydrolysis of a Nerve-Agent

Simulant. *ACS Appl. Nano Mater.* **2019**, *2* (2), 1005–1008. https://doi.org/10.1021/acsanm.8b02292.

(28) Aum Shinrikyo: Images from the 1995 Tokyo Sarin Attack. *BBC News*. July 6, 2018. https://www.bbc.com/news/in-pictures-43629706 (accessed 2023-05-10).

(29) Hubbard, B. Dozens Suffocate in Syria as Government Is Accused of Chemical Attack. *The New York Times*. April 8, 2018. https://www.nytimes.com/2018/04/08/world/middleeast/syria-chemical-attack-ghouta.html (accessed 2023-05-10).

(30) Enserink, M. U.N. Taps Special Labs to Investigate Syrian Attack. *Science* **2013**, *341* (6150), 1050–1051. https://doi.org/10.1126/science.341.6150.1050.

(31) *U.S. concerned Russia could use chemical weapons in Ukraine - POLITICO*. https://www.politico.com/news/2022/11/23/russia-chemical-weapons-ukraine-00070743 (accessed 2025-03-19).

(32) Li, Y.; Yan, J.; Yu, D.; Lei, P.; Shen, W.; Zhong, M.; Zhang, J.; Guo, S. Hydrolysis of Organophosphorus Agents Catalyzed by Cobalt Nanoparticles Supported on Three-Dimensional Nitrogen-Doped Graphene. *Inorg. Chem.* **2021**, *60* (23), 17635–17640. https://doi.org/10.1021/acs.inorgchem.1c02217.

(33) Osovsky, R.; Kaplan, D.; Nir, I.; Rotter, H.; Elisha, S.; Columbus, I. Decontamination of Adsorbed Chemical Warfare Agents on Activated Carbon Using Hydrogen Peroxide Solutions. *Environ. Sci. Technol.* **2014**, *48* (18), 10912–10918. https://doi.org/10.1021/es502981y.

(34) Ploskonka, A. M.; DeCoste, J. B. Insight into Organophosphate Chemical Warfare Agent Simulant Hydrolysis in Metal-Organic Frameworks. *J. Hazard. Mater.* **2019**, *375*, 191–197. https://doi.org/10.1016/j.jhazmat.2019.04.044.

(35) Liao, Y.; Sheridan, T.; Liu, J.; Farha, O.; Hupp, J. Product Inhibition and the Catalytic Destruction of a Nerve Agent Simulant by Zirconium-Based Metal–Organic Frameworks. *ACS Appl. Mater. Interfaces* **2021**, *13* (26), 30565–30575. https://doi.org/10.1021/acsami.1c05062.

(36) Helm, L.; Merbach, A. E. Water Exchange on Metal Ions: Experiments and Simulations. *Coord. Chem. Rev.* **1999**, *187* (1), 151–181. https://doi.org/10.1016/S0010-8545(99)90232-1.

(37) Lincoln, S. F. Mechanistic Studies of Metal Aqua Ions: A Semi-Historical Perspective. *Helv. Chim. Acta* **2005**, *88* (3), 523–545. https://doi.org/10.1002/hlca.200590036.

(38) Tai, T.-Y.; Sha, F.; Wang, X.; Wang, X.; Ma, K.; Kirlikovali, K. O.; Su, S.; Islamoglu, T.; Kato, S.; Farha, O. K. Leveraging Isothermal Titration Calorimetry to Explore Structure–Property Relationships of Protein Immobilization in Metal–Organic Frameworks. *Angew. Chem. Int. Ed.* **2022**, *61* (37), e202209110. https://doi.org/10.1002/anie.202209110.

(39) Sha, F.; Xie, H.; Son, F. A.; Kim, K. S.; Gong, W.; Su, S.; Ma, K.; Wang, X.; Wang, X.; Farha, O. K. Rationally Tailored Mesoporous Hosts for Optimal Protein Encapsulation. *J. Am. Chem. Soc.* **2023**, *145* (30), 16383–16390. https://doi.org/10.1021/jacs.3c01989.

(40) Torres, C.; Potts, D. S.; Flaherty, D. W. Solvent Mediated Interactions on Alkene Epoxidations in Ti-MFI: Effects of Solvent Identity and Silanol Density. *ACS Catal.* **2023**, *13* (13), 8925–8942. https://doi.org/10.1021/acscatal.3c01073.

(41) Fahy, K. M.; Sha, F.; Reischauer, S.; Lee, S.; Tai, T.-Y.; Farha, O. K. Role of Metal–Organic Framework Topology on Thermodynamics of Polyoxometalate Encapsulation. *ACS Appl. Mater. Interfaces* **2024**, *16* (23), 30296–30305. https://doi.org/10.1021/acsami.4c05016.

(42) Drout, R. J.; Kato, S.; Chen, H.; Son, F. A.; Otake, K.; Islamoglu, T.; Snurr, R. Q.; Farha, O. K. Isothermal Titration Calorimetry to Explore the Parameter Space of Organophosphorus Agrochemical Adsorption in MOFs. *J. Am. Chem. Soc.* **2020**, *142* (28), 12357–12366. https://doi.org/10.1021/jacs.0c04668.

(43) Fahy, K. M.; Lee, S.; Akpinar, I.; Sha, F.; Ahmadi Khoshooei, M.; Su, S.; Islamoglu, T.; Gianneschi, N. C.; Farha, O. K. Thermodynamic Insights into Phosphonate Binding in Metal–Azolate Frameworks. *J. Am. Chem. Soc.* **2024**, *146* (8), 5661–5668. https://doi.org/10.1021/jacs.3c14643.

(44) Islamoglu, T.; Otake, K.; Li, P.; Buru, C. T.; Peters, A. W.; Akpinar, I.; Garibay, S. J.; Farha, O. K. Revisiting the Structural Homogeneity of NU-1000, a Zr-Based Metal–Organic Framework. *CrystEngComm* **2018**, *20* (39), 5913–5918. https://doi.org/10.1039/C8CE00455B.

(45) Beyzavi, H.; Klet, R. C.; Tussupbayev, S.; Borycz, J.; Vermeulen, N. A.; Cramer, C. J.; Stoddart, J. F.; Hupp, J. T.; Farha, O. K. A Hafnium-Based Metal–Organic Framework as an Efficient and Multifunctional Catalyst for Facile CO2 Fixation and Regioselective and Enantioretentive Epoxide Activation. *J. Am. Chem. Soc.* **2014**, *136* (45), 15861–15864. https://doi.org/10.1021/ja508626n.

(46) Mian, M. R.; Islamoglu, T.; Afrin, U.; Goswami, S.; Cao, R.; Kirlikovali, K. O.; Hall, M. G.; Peterson, G. W.; Farha, O. K. Catalytic Degradation of an Organophosphorus Agent at

Zn–OH Sites in a Metal–Organic Framework. *Chem. Mater.* **2020**, *32* (16), 6998–7004. https://doi.org/10.1021/acs.chemmater.0c02373.

(47) Mian, M. R.; Chen, H.; Cao, R.; Kirlikovali, K. O.; Snurr, R. Q.; Islamoglu, T.; Farha, O. K. Insights into Catalytic Hydrolysis of Organophosphonates at M–OH Sites of Azolate-Based Metal Organic Frameworks. *J. Am. Chem. Soc.* **2021**, *143* (26), 9893–9900. https://doi.org/10.1021/jacs.1c03901.

(48) Simon, M. A.; Anggraeni, E.; Soetaredjo, F. E.; Santoso, S. P.; Irawaty, W.; Thanh, T. C.; Hartono, S. B.; Yuliana, M.; Ismadji, S. Hydrothermal Synthesize of HF-Free MIL-100(Fe) for Isoniazid-Drug Delivery. *Sci. Rep.* **2019**, *9* (1), 16907. https://doi.org/10.1038/s41598-019-53436-3.

(49) Idrees, K. B.; Li, Z.; Xie, H.; Kirlikovali, K. O.; Kazem-Rostami, M.; Wang, X.; Wang, X.; Tai, T.-Y.; Islamoglu, T.; Stoddart, J. F.; Snurr, R. Q.; Farha, O. K. Separation of Aromatic Hydrocarbons in Porous Materials. *J. Am. Chem. Soc.* **2022**, *144* (27), 12212–12218. https://doi.org/10.1021/jacs.2c03114.

(50) Wang, J. Thermodynamic Equilibrium and Kinetic Fundamentals of Oxide Dissolution in Aqueous Solution. *J. Mater. Res.* **2020**, *35* (8), 898–921. https://doi.org/10.1557/jmr.2020.81.

(51) Cen, S.; Li, L.; Li, Y.; Wan, C.; Linghu, W.; Wang, L. Low-Temperature Catalytic Transfer Hydrogenation of Biomass-Derived Furfural over Irreversibly Adsorbed and Highly Dispersed Zr(IV) Species. *Inorg. Chem.* **2024**, *63* (29), 13775–13784. https://doi.org/10.1021/acs.inorgchem.4c02156.

(52) Lyu, J.; Zhang, X.; Li, P.; Wang, X.; Buru, C. T.; Bai, P.; Guo, X.; Farha, O. K. Exploring the Role of Hexanuclear Clusters as Lewis Acidic Sites in Isostructural Metal–Organic

Frameworks. *Chem. Mater.* **2019**, *31* (11), 4166–4172. https://doi.org/10.1021/acs.chemmater.9b00960.

(53) Rimoldi, M.; Howarth, A. J.; DeStefano, M. R.; Lin, L.; Goswami, S.; Li, P.; Hupp, J. T.; Farha, O. K. Catalytic Zirconium/Hafnium-Based Metal–Organic Frameworks. *ACS Catal.* **2017**, *7* (2), 997–1014. https://doi.org/10.1021/acscatal.6b02923.

(54) Komanoya, T.; Nakajima, K.; Kitano, M.; Hara, M. Synergistic Catalysis by Lewis Acid and Base Sites on ZrO2 for Meerwein–Ponndorf–Verley Reduction. *J. Phys. Chem. C* **2015**, *119* (47), 26540–26546. https://doi.org/10.1021/acs.jpcc.5b08355.

(55) Horcajada, P.; Surblé, S.; Serre, C.; Hong, D.-Y.; Seo, Y.-K.; Chang, J.-S.; Grenèche, J.-M.; Margiolaki, I.; Férey, G. Synthesis and Catalytic Properties of MIL-100(Fe), an Iron(III) Carboxylate with Large Pores. *Chem. Commun.* **2007**, No. 27, 2820–2822. https://doi.org/10.1039/B704325B.

(56) Klet, R. C.; Liu, Y.; Wang, T. C.; Hupp, J. T.; Farha, O. K. Evaluation of Brønsted Acidity and Proton Topology in Zr- and Hf-Based Metal–Organic Frameworks Using Potentiometric Acid–Base Titration. *J. Mater. Chem. A* **2016**, *4* (4), 1479–1485. https://doi.org/10.1039/C5TA07687K.

(57) Syed, Z. H.; Mian, M. R.; Patel, R.; Xie, H.; Pengmei, Z.; Chen, Z.; Son, F. A.; Goetjen, T. A.; Chapovetsky, A.; Fahy, K. M.; Sha, F.; Wang, X.; Alayoglu, S.; Kaphan, D. M.; Chapman, K. W.; Neurock, M.; Gagliardi, L.; Delferro, M.; Farha, O. K. Sulfated Zirconium Metal–Organic Frameworks as Well-Defined Supports for Enhancing Organometallic Catalysis. *J. Am. Chem. Soc.* **2022**, *144* (37), 16883–16897. https://doi.org/10.1021/jacs.2c05290.

(58) Jiang, J.; Gándara, F.; Zhang, Y.-B.; Na, K.; Yaghi, O. M.; Klemperer, W. G. Superacidity in Sulfated Metal–Organic Framework-808. *J. Am. Chem. Soc.* **2014**, *136* (37), 12844–12847. https://doi.org/10.1021/ja507119n.

(59) Bornes, C.; Fischer, M.; Amelse, J. A.; Geraldes, C. F. G. C.; Rocha, J.; Mafra, L. What Is Being Measured with P-Bearing NMR Probe Molecules Adsorbed on Zeolites? *J. Am. Chem. Soc.* **2021**, *143* (34), 13616–13623. https://doi.org/10.1021/jacs.1c05014.

(60) Zheng, A.; Zhang, H.; Lu, X.; Liu, S.-B.; Deng, F. Theoretical Predictions of 31P NMR Chemical Shift Threshold of Trimethylphosphine Oxide Absorbed on Solid Acid Catalysts. *J. Phys. Chem. B* **2008**, *112* (15), 4496–4505. https://doi.org/10.1021/jp709739v.

ASSOCIATED CONTENT

Supporting Information

Experimental procedures and characterization data. This material is available free of charge via the Internet at http://pubs.acs.org.

Materials and general procedures, PXRD, N_2 isotherms, SEM images, POM characterization, EDS mapping data, ITC thermograms and binding curves for NU-901, NU-903, NU-1200, and blank titrations.

The Supporting Information is available free of charge on the ACS Publications website.

AUTHOR INFORMATION

Corresponding Author

*o-farha@northwestern.edu

Notes

O.K.F. has a financial interest in NuMat Technologies, a start-up seeking to commercialize MOFs.

ACKNOWLEDGEMENTS

O.K.F. gratefully acknowledges support from the Defense Threat Reduction Agency (HDTRA1-19-1-0007) and the Catalyst Design for Decarbonization Center, an Energy Frontier Research Center, which is funded by the US Department of Energy (DOE), Office of Science, Basic Energy Sciences (BES) DE-SC0023383. This work made use of the IMSERC X-RAY facility at Northwestern University, which has received support from the Soft and Hybrid Nanotechnology Experimental (SHyNE) Resource (NSF ECCS-2025633), and Northwestern University. This work also made use of the EPIC facility of Northwestern University's NU Center, which has received support from the SHyNE Resource (NSF ECCS-2025633), the IIN, and Northwestern's MRSEC program (NSF DMR-1720139). C.S. and S.L. gratefully acknowledge support from the Ryan Fellowship and the International Institute for Nanotechnology at Northwestern University. K.M.F. is supported by the National Science Foundation Graduate Research Fellowship (NSF GRFP) under Grant No. DGE-1842165.